surfaces

MDPI

Article

PET-Derived Nanoporous Carbon–MnO_2 Hybrid Electrodes for Supercapacitors: Influence of Electrolyte on Charge Storage Mechanisms

Dipendu Saha [1,*], Lindsay Lapointe [1], Kurt W. Kolasinski [2] and Carley M. Beam [1]

[1] Chemical and Materials Engineering Department, Widener University, 1 University Place, Chester, PA 19013, USA; lmlapointe@widener.edu (L.L.); cmbeam@widener.edu (C.M.B.)
[2] Department of Chemistry, West Chester University, West Chester, PA 19383, USA; kkolasinski@wcupa.edu
* Correspondence: dsaha@widener.edu; Tel.: +1-610-499-4056; Fax: +1-610-499-4059

Abstract

The increasing accumulation of poly(ethylene terephthalate) (PET) waste poses a significant environmental challenge and highlights the need for sustainable, value-added recycling strategies. In this study, porous carbon derived from PET was synthesized via carbonization and chemical activation and subsequently combined with manganese dioxide (MnO_2) to fabricate hybrid electrodes for aqueous supercapacitors. The PET-derived carbon exhibits a highly microporous structure with a large specific surface area and functions as a conductive and mechanically stable matrix that improves MnO_2 dispersion, charge transport, and electrochemical utilization. Systematic electrochemical investigations reveal strongly electrolyte-dependent charge-storage behavior. In an alkaline electrolyte, the capacitance is dominated by MnO_2 pseudocapacitive redox reactions, whereas in a neutral electrolyte, the response is primarily governed by electric double-layer charge storage. In a ferricyanide-containing redox-active electrolyte, additional electrolyte-mediated faradaic processes significantly enhance the apparent electrochemical performance. Under these conditions, the hybrid electrodes deliver a high apparent specific capacitance of 240–250 F g^{-1} at moderate current densities. The electrodes further demonstrate stable cycling behavior and high apparent Coulombic efficiency, reflecting time-dependent utilization of both MnO_2 pseudocapacitance and redox-active electrolyte species during charge–discharge. Crucially, this work demonstrates that PET-derived carbon/MnO_2 hybrid electrodes exhibit complex, electrolyte-controlled charge-storage mechanisms and underscores the critical role of electrolyte selection in accurately interpreting electrochemical metrics and optimizing the performance of sustainable supercapacitors based on recycled polymer-derived carbons.

Keywords: PET waste recycling; supercapacitors; porous carbon; manganese dioxide (MnO_2); redox-active electrolyte

Check for updates

Academic Editors: Siwen Zhang and Bosi Yin

Received: 25 March 2026
Revised: 24 April 2026
Accepted: 24 April 2026
Published: 30 April 2026

Copyright: © 2026 by the authors. Licensee MDPI, Basel, Switzerland. This article is an open access article distributed under the terms and conditions of the Creative Commons Attribution (CC BY) license.

1. Introduction

Poly(ethylene terephthalate) (PET) is one of the most widely used polymers, especially in packaging and textiles, and its massive consumption has created a persistent solid-waste burden because post-consumer PET is generated in large volumes and is not fully recovered through conventional recycling streams. Even where collection exists, downcycling, contamination, and economics limit closed-loop reuse, motivating alternative routes that can convert PET waste into higher-value products while supporting circular-economy goals. Recent reviews of PET recycling technologies emphasize both the urgency of improving

PET recovery and the need for scalable, low-cost pathways that reduce environmental impact relative to virgin production [1–4]. In this context, upcycling PET into functional carbon materials is particularly attractive because it can simultaneously address waste mitigation and supply-chain needs for electrochemical energy-storage electrodes. Indeed, polymer-waste-derived carbons have emerged as a rapidly growing family of materials for electrochemical devices, with recent reviews highlighting how feedstock selection and conversion conditions strongly influence carbon microstructure, conductivity, and surface chemistry [5].

Electrochemical supercapacitors occupy a critical niche between conventional dielectric capacitors and batteries because they can deliver high power density, fast charge–discharge, and long cycle life, making them relevant for regenerative braking, power buffering, and hybrid energy systems. The performance of supercapacitors is governed primarily by electrode materials and electrolyte chemistry; among electrode choices, carbon materials remain dominant due to their electrical conductivity, chemical stability in aqueous electrolytes, tunable surface chemistry, and manufacturability in practical electrode architectures. Comprehensive reviews have detailed how carbons—ranging from activated carbons to graphene-based and heteroatom-doped carbons—store charge through electric double-layer capacitance (EDLC) and how pore structure controls ion accessibility and rate capability [6]. Importantly, polymer waste-derived carbons (including those derived from PET) are increasingly studied as sustainable electrode candidates, and recent work has demonstrated that PET waste can be converted into carbonaceous materials suitable for supercapacitor electrodes, supporting the feasibility of PET-to-electrode value chains [7–11].

While EDLC-based carbons excel in power and stability, their energy density is often limited, which has driven major interest in pseudocapacitance—fast, reversible faradaic charge storage associated with surface or near-surface redox processes. Among pseudocapacitive materials, manganese dioxide (MnO_2) is widely investigated because of its low cost, environmental compatibility, and high theoretical capacitance; however, practical utilization is frequently constrained by modest intrinsic electronic conductivity and ion-transport limitations, particularly when MnO_2 domains become electrically isolated or when electrolyte ions cannot effectively access redox-active sites [12–17]. Consequently, a common and effective design strategy is to construct hybrid electrodes in which a conductive carbon scaffold provides rapid electron pathways and high surface area, while MnO_2 contributes pseudocapacitance. Extensive prior studies and reviews show that MnO_2/carbon composites can outperform either component alone by improving MnO_2 dispersion, reducing charge-transfer resistance, and enhancing rate capability [18,19]. In parallel, electrolyte engineering—especially the use of redox-active additives such as ferricyanide/ferrocyanide—has been demonstrated to boost apparent charge storage by providing an additional reversible redox reservoir in the electrolyte, thereby increasing stored charge and extending discharge time under galvanostatic operation [20–23], including pure MnO_2-based systems [24].

In this work, we investigate hybrid supercapacitor electrodes composed of PET-derived nonporous carbon and MnO_2, and systematically examine how their charge-storage behavior is influenced by multiple electrolyte chemistries, including neutral sulfate electrolyte and ferricyanide-containing redox-active formulations. Building on prior demonstrations of PET-waste-derived carbons as viable supercapacitor electrodes [7–9] and the established synergy between MnO_2 and conductive carbon frameworks [18,19], this study focuses on mechanistically clarifying how electrode composition (carbon/MnO_2 fraction) and electrolyte selection together determine electrochemical signatures, including the frequently observed divergence between CV- and GCD-derived capacitance in redox-active systems. Consistent with literature indicating that ferricyanide additives can shift devices

toward redox-mediated behavior, our results provide insight into (i) the relative contributions of EDLC, MnO_2 pseudocapacitance, and electrolyte redox processes and (ii) how these contributions evolve across measurement time scales and electrolyte environments. Overall, the manuscript aims to shed light on PET-derived carbon/MnO_2 hybrid electrodes as a sustainable materials platform and to establish electrolyte-dependent design rules for interpreting and optimizing their supercapacitor performance.

2. Experimental

2.1. Synthesis of Porous Carbons from PET

Post-consumer PET plastic waste was first manually cleaned by removing labels and caps, after which the material was cut into fragments measuring approximately 2–3 cm. The prepared PET pieces were loaded into a porcelain boat and placed inside a Lindberg/Blue M tube furnace for carbonization. The temperature was ramped to 500 °C at a heating rate of 10 °C min^{-1} and then allowed to cool naturally to ambient temperature. Throughout the thermal treatment, a continuous flow of nitrogen gas was maintained to ensure an inert atmosphere and suppress oxidative degradation. The resultant carbon was activated using a chemical activation technique [25–27]. Typically, the resulting carbonized product was subsequently blended with solid sodium hydroxide (NaOH) at carbon-to-NaOH weight ratios of 1:3 and subjected to chemical activation using the same tube furnace. Activation was carried out by heating the mixtures to 1000 °C at 10 °C min^{-1}, holding at the target temperature for 1 min, and then cooling to room temperature under nitrogen flow. Following activation, the samples were thoroughly washed multiple times with deionized water, filtered, and dried in an oven at 100 °C overnight.

2.2. Materials Characterization of Porous Carbon MnO_2

The synthesized carbon and as-received commercial MnO_2 were characterized for their pore textural properties, morphology, and surface chemistry. Nitrogen (N_2) adsorption–desorption isotherms at 77 K and carbon dioxide (CO_2) adsorption at 273 K were measured using a Autosorb-iQ gas sorption analyzer (Anton Paar, formerly Quantachrome, Boynton Beach, FL, USA) to determine surface area and porosity. Scanning electron microscopy (SEM) images were obtained using a Apreo 2S LoVac SEM (ThermoScientific, Waltham, MA, USA). Energy-dispersive X-ray spectroscopy (EDS) analyses were performed in this same instrument with an xMax detector (Oxford Instruments, Santa Barbara, CA, USA) and AZtech 6.3 analysis software.

2.3. Fabrication of Supercapacitor Electrodes and Testing

Porous carbons were synthesized from PET waste as mentioned above, whereas MnO_2 was obtained from commercial sources (Millipore Sigma, Burlington, MA, USA). The hybrid electrodes were made with six different compositions of porous carbons and MnO_2, e.g., 0%, 20%, 40%, 60%, 80%, and 100% of porous carbon.

Electrode fabrication was carried out using polyvinylidene fluoride (PVDF) as the binder, which was first dissolved in N,N-dimethylacetamide (DMAc) to prepare a 5 wt.% solution. The activated carbon/MnO_2 mixture was initially ground using a ball mill and then combined with Super P conductive carbon black and the PVDF solution at a weight ratio of 8:1:1 (carbon/MnO_2:PVDF:Super P). To adjust the slurry viscosity, a small amount of acetone was added, followed by ultrasonication to ensure uniform dispersion. Commercial graphite foil was used as the current collector for all assembled supercapacitor devices. The drop-casting method was used to apply the coating on the graphite foil.

All electrochemical characterizations were carried out using a BASi PalmSens3 potentiostat. Three types of electrolytes were employed: (i) 6 M KOH solution, (ii) 1 M Na_2SO_4

solution, and (iii) a mixture of 1 M Na_2SO_4 and 0.03 M $K_3[Fe(CN)_6)]$. Cyclic voltammetry measurements were performed in a three-electrode setup, with the carbon-coated miniature electrode serving as the working electrode, an Ag/AgCl electrode as the reference, and a platinum wire as the counter electrode. CV tests were conducted at scan rates of 10, 20, 30, 40, 50, and 75 mV/s in all the electrolytes. Galvanostatic charge–discharge (GCD) experiments were performed in the instrument with a current density of 0.1 A/g. Electrochemical impedance spectroscopy (EIS) was conducted by sweeping the frequency from 1 Hz to 1 MHz to investigate the impedance characteristics of the devices.

3. Results and Discussions

3.1. Materials Characteristics

The N_2 adsorption–desorption isotherm at 77 K is shown in Figure 1a, and the pore-size distribution is shown in Figure 1b for PET-derived porous carbon and MnO_2. As can be observed in Figure 1a, the N_2 adsorption–desorption plot is type 1 with no visible hysteresis. This suggests that the PET-derived porous carbon is primarily a microporous material. On the other hand, the amount of nitrogen in the adsorption–desorption isotherm for MnO_2 is very low and certainly demonstrates a practically nonporous material. The total pore volume of the carbon and MnO_2 is 0.57 and 0.015 cm^3/g, respectively. The BET specific surface area for porous carbon is 1150 m^2/g, whereas for MnO_2, the BET surface area is no more than 2.65 m^2/g. The NLDFT-based pore-size distribution suggests that the key pore of the carbon is within 10 Å with no practical porosity after 20 Å. The pore textural properties are provided in Table 1.

The X-ray diffraction data are shown in Figure 2. For PET-derived carbon, the hump-like disordered peaks appear at 23° and 43° in the XRD pattern. These peaks are the remnants of graphite-like sp^2 structures and represent (002) and (101) reflexes. These are observed for most of the produced carbon materials, for which the (002) peak is most common and signifies stacking of graphite-like planes. For MnO_2, however, there are several sharp peaks observed. The largest peak is observed at around a 30° angle, which originates from a (110) reflection. The other larger peaks observed at around 38°, 57°, 60° and 72°, which represent (101), (111), (211) and (112) reflections, are followed by a few minor peaks. The XRD pattern of the manganese dioxide film suggests that it is closely associated with the $\beta-MnO_2$ structure (rutile, ICDD/JCPDS database (PDF No. 44-0141)) and has a crystallite size of around 22.2 nm [13,28].

The SEM micrograph is presented in Figure 3, and the corresponding energy-dispersive X-ray spectroscopy (EDS) results are shown in Figure 4. The PET-derived carbon particles exhibit a wide distribution of sizes and irregular shapes, ranging from a few micrometers to over 100 µm. After mixing the porous carbon with carbon black and MnO_2 in the presence of PVDF through grinding, the particle sizes are significantly reduced. The SEM image indicates effective and uniform mixing among the components. The smaller particles are primarily attributed to carbon black and manganese dioxide, while the larger particles correspond to the porous carbon. EDS analysis of the composite electrode deposited on a graphite strip reveals a carbon content of approximately 56% and a manganese content of about 20%. A substantial oxygen signal is also observed, originating from both MnO_2 and the carbon framework, while fluorine is associated with the PVDF binder. In addition, trace amounts of Na, Al, Si, Cl, S, Ca, and Cu are detected, which are attributed to impurities from the precursor chemicals as well as from the porcelain/alumina boats used during the carbonization and activation processes. The detailed elemental composition is summarized in Table 1. It should be noted that SEM imaging cannot resolve microporosity in disordered carbon materials, as its resolution is limited to much larger

length scales. Therefore, the smooth surface observed in SEM does not contradict the high surface area and microporosity derived from BET analysis.

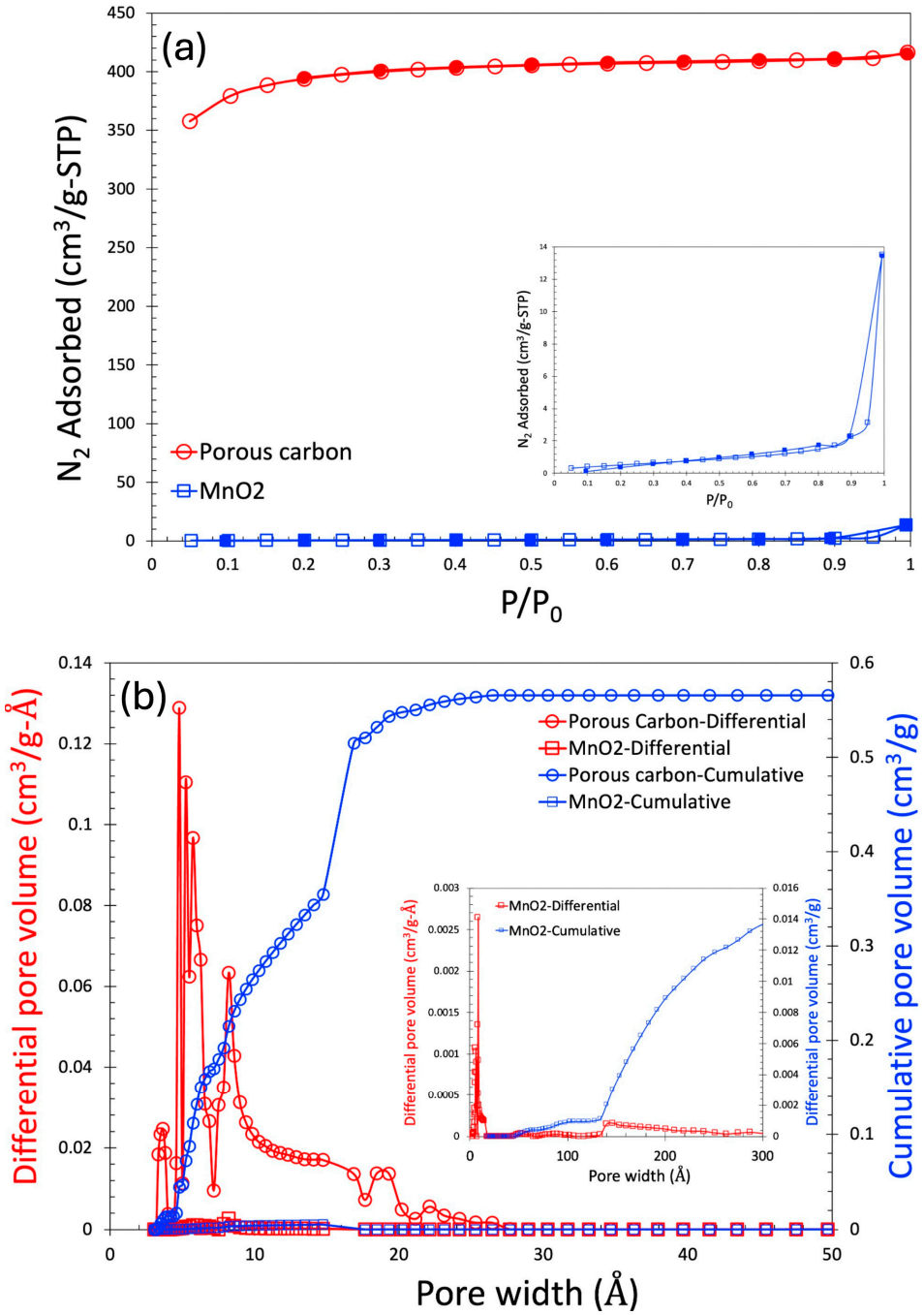

Figure 1. N_2 adsorption–desorption plot at 77 K (**a**) and pore-size distribution obtained from N_2 adsorption at 77 K and CO_2 adsorption at 273 K (**b**). The inset picture in (**a**) shows the magnified view of N_2 adsorption on MnO_2.

Table 1. Composition of carbon/MnO_2 composite (PET-derived carbon = 40%) obtained from SEM-EDS. Atomic percent values were obtained by averaging over the full rectangular region of the images in Figure 4. These values can be used to confirm the presence of the elements detected, but for such heterogeneous samples, they should not be considered as true stoichiometric ratios.

Elements	C	O	F	Na	Al	Si	S	Cl	Ca	Mn	Cu
At.%	56.4	21.7	4.48	0.41	0.03	0.07	0.07	0.15	0.05	20.4	0.12

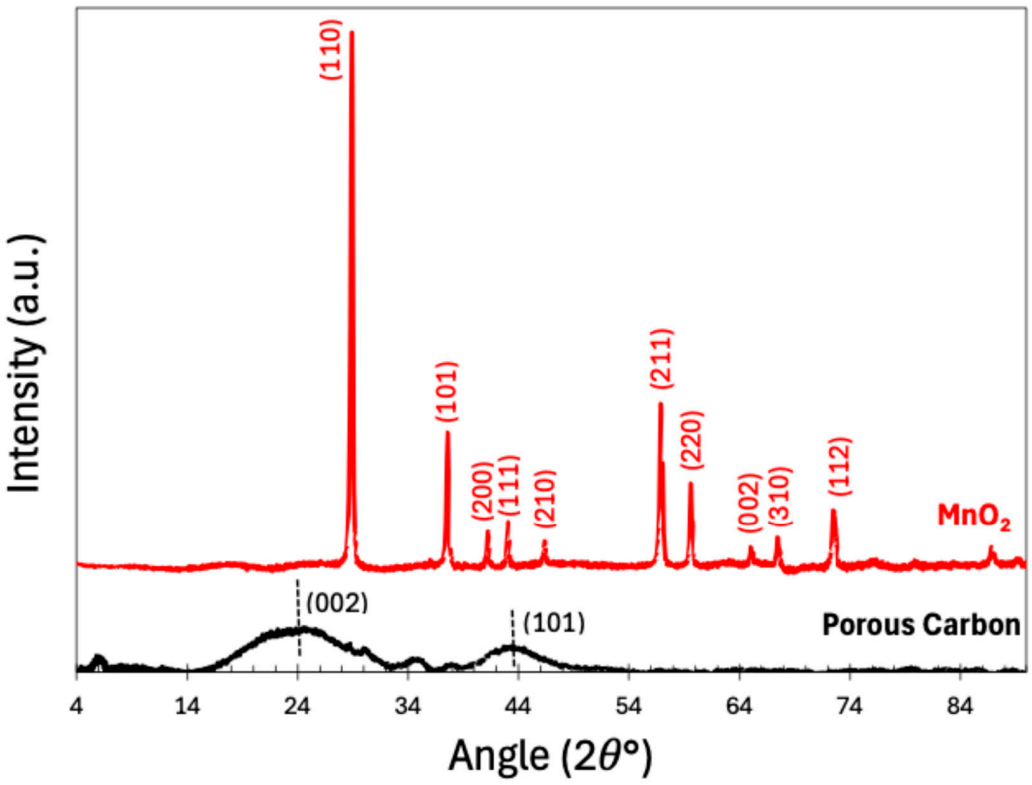

Figure 2. X-ray diffraction (XRD) patterns of PET-derived carbon and MnO_2.

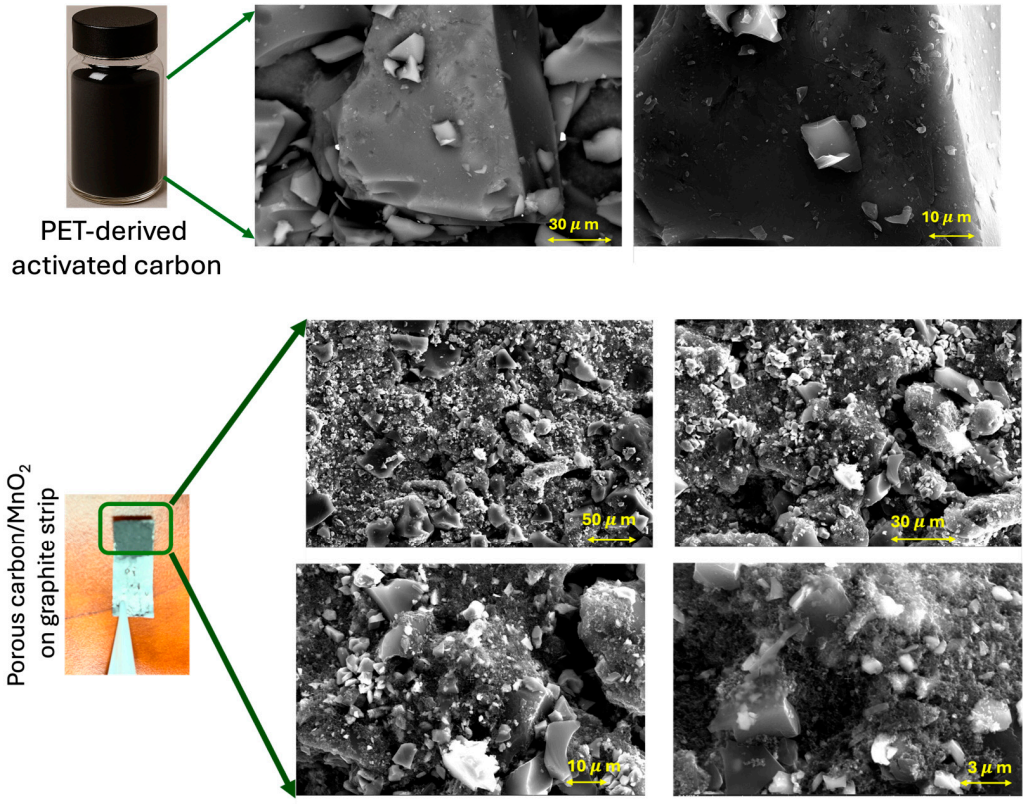

Figure 3. Back-scattered electron SEM images of PET-derived porous carbon (**upper** panels) and porous carbon/MnO_2 composite (**lower** panels) on a graphite strip in different levels of magnification. The various topographies shown have been selected to demonstrate the heterogeneous nature of the samples.

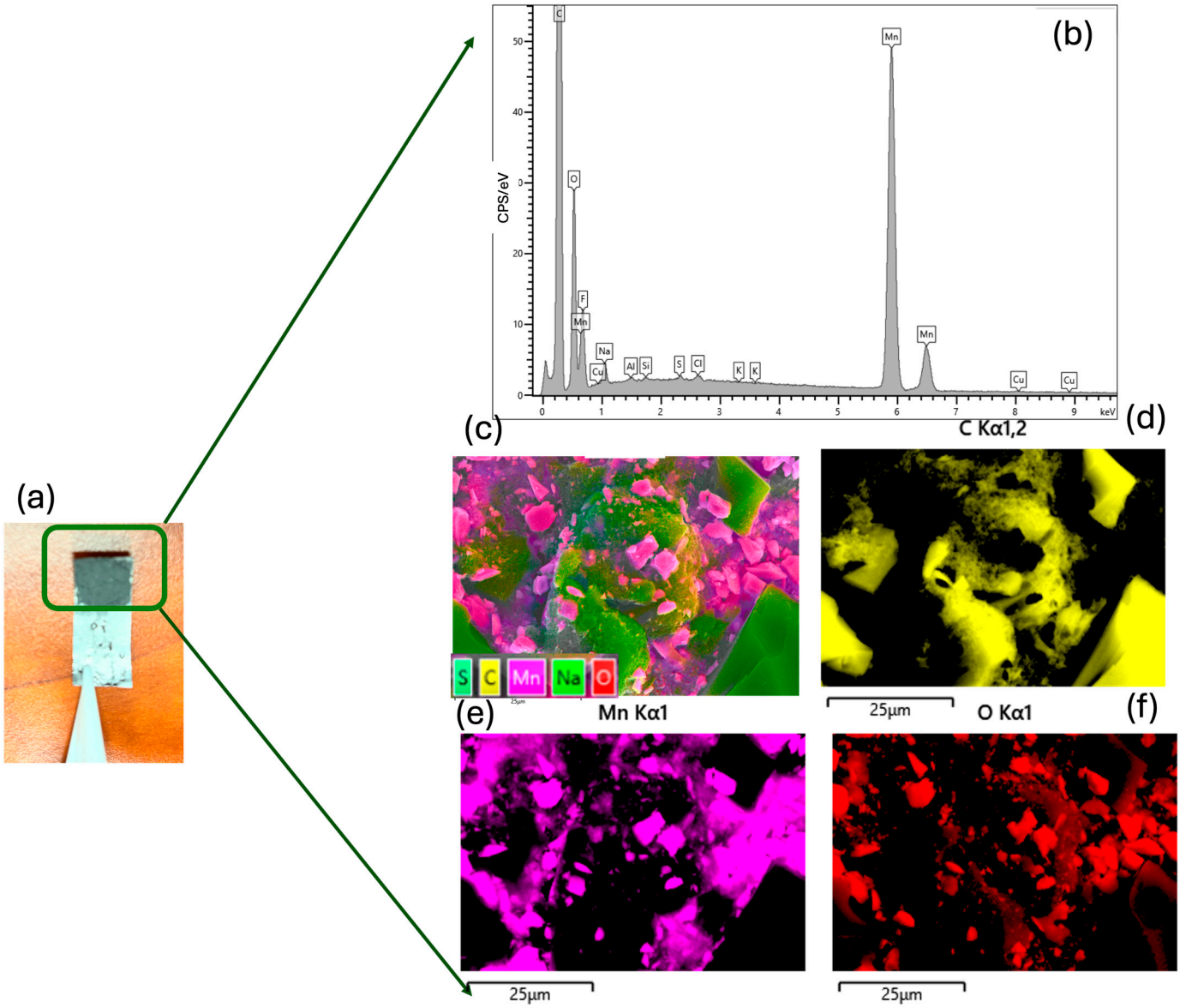

Figure 4. SEM-EDS mapping of porous carbon/MnO_2 composite on graphite strip. False-color imaging is used to highlight the heterogeneous distribution of different elements in the sample. (**a**) Carbon-coated electrode area in which EDS spectra were collected. (**b**) Spectroscopic representation of elemental composition. (**c**) A composite image color-coded to differentiate the locations of S, C, Mn, Na and O. (**d**) An elemental map showing the prevalence of C in the sample. (**e**) An elemental map showing the prevalence of Mn in the sample. (**f**) An elemental map showing the prevalence of O in the sample.

3.2. Electrochemical Behavior

The cyclic voltammetry plots in 6 M KOH, 1 M Na_2SO_4, and the mixture of 1 M Na_2SO_4 and 0.03 M $K_3[Fe(CN)_6]$ are shown in Figure 5a–c, respectively, for the scan rates of 10, 20, 30, 40, 50, and 75 mV/s in all the compositions of porous carbon MnO_2. Specific pseudocapacitance peaks originating from the MnO_2 are observed in all compositions except 100% carbon for KOH-based electrolyte and 0–40% carbon for the mixture of Na_2SO_4 and $K_3[Fe(CN)_6]$-based electrolytes; no such peaks are observed in pure Na_2SO_4-based electrolytes. It can also be observed that, at high scan rates for the KOH-based electrolyte, a few of the CV plots are truncated as they exceed the maximum current range of the instrument.

In alkaline electrolytes such as KOH, MnO_2 typically exhibits pseudocapacitance through fast, reversible faradaic processes occurring at or near the surface, coupled with

cation insertion/extraction and/or surface adsorption. The alkaline environment generally provides high ionic conductivity and facilitates rapid charge compensation, which can improve apparent capacitance and rate capability relative to many neutral electrolytes (though the exact behavior depends strongly on MnO_2 phase, hydration, crystallinity, and loading). Mechanistically, the redox chemistry is commonly described as the Mn(IV)/Mn(III) redox couple, with charge balance achieved by electrolyte cations (K^+) and/or protons associated with structural water/hydroxylated surface groups.

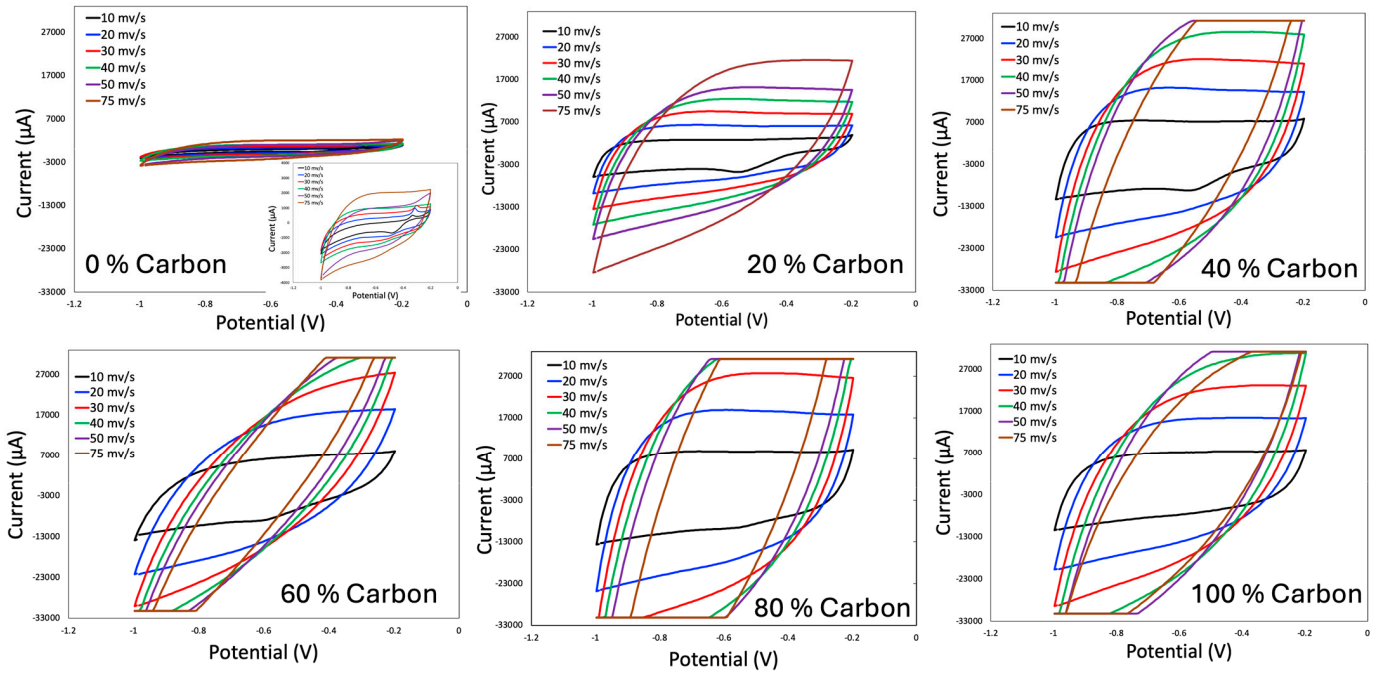

(**a**)

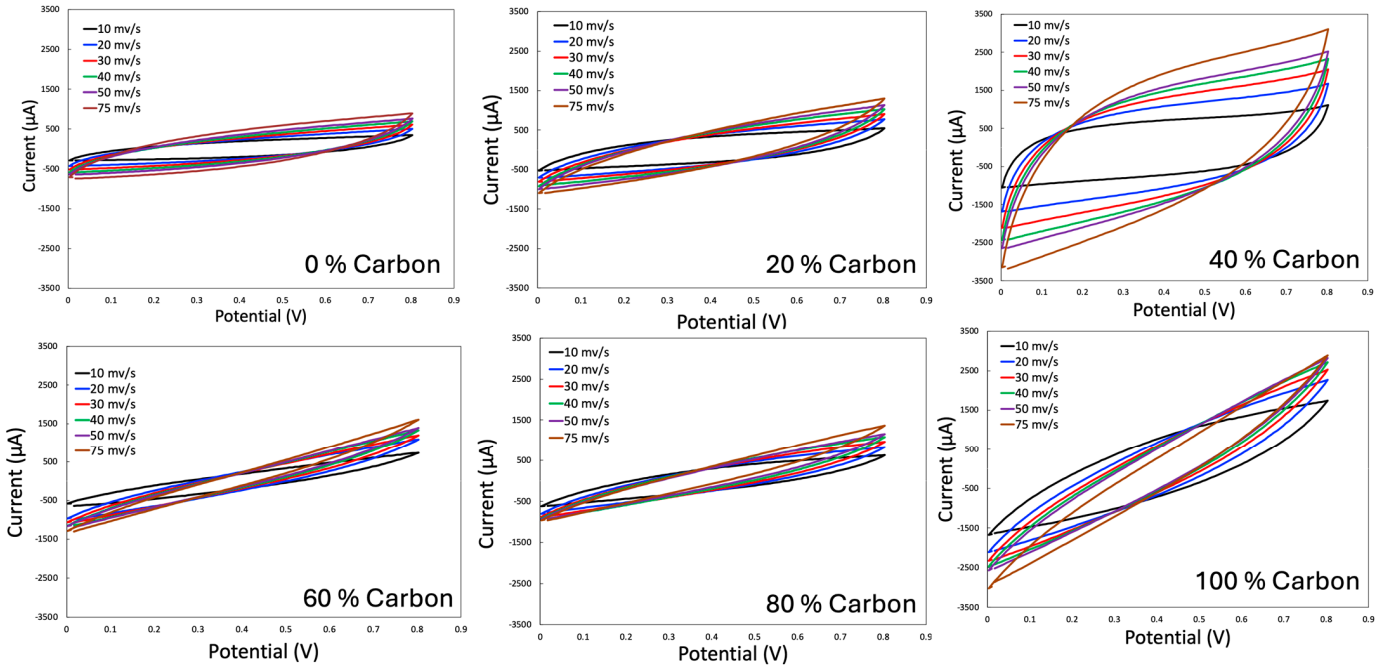

(**b**)

Figure 5. *Cont.*

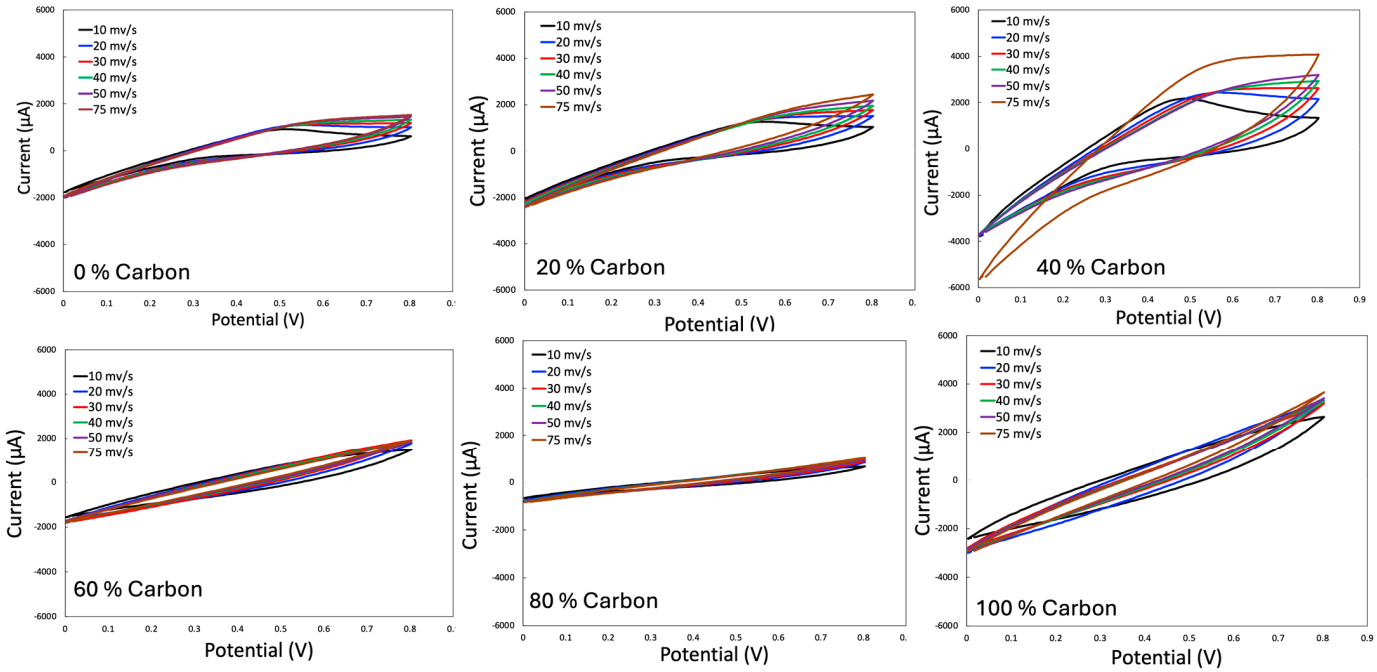

(**c**)

Figure 5. (**a**) Cyclic voltammetry (CV) plots in KOH as electrolyte. (**b**) Cyclic voltammetry (CV) plots in $NaSO_4$ as electrolyte. (**c**) Cyclic voltammetry (CV) plots in the mixture of Na_2SO_4 and $K_3[Fe(CN)_6]$ as electrolyte.

A widely used simplified representation in alkaline media is the K^+-assisted surface/insertion reaction. This scheme is frequently used to describe K^+ insertion/extraction (or adsorption/desorption with partial insertion) as the charge-compensation mechanism during Mn reduction/oxidation in KOH [15].

$$MnO_2 + K^+ + e^- \rightleftharpoons MnOOK \quad (1)$$

In addition to K^+ participation, many MnO_2 materials exhibit proton-coupled processes even in non-acidic electrolytes, often written generically as

$$MnO_2 + H^+ + e^- \rightleftharpoons MnOOH \quad (2)$$

In practice, the "H^+" term is often interpreted as proton activity associated with surface –OH groups and structural/adsorbed water, rather than free protons in bulk alkaline solution. The broader idea—pseudocapacitance via reversible Mn valence changes compensated by cations (including K^+) and/or protons—is discussed in mechanistic overviews of MnO_2 electrochemical capacitors [11,29,30].

In neutral "mild" electrolytes such as Na_2SO_4, MnO_2 pseudocapacitance is classically described as surface/near-surface redox accompanied by insertion (or adsorption) of cations from the electrolyte—here, primarily Na^+—and frequently with co-participation of protons (again, often from structural/adsorbed water rather than high bulk $[H^+]$). The key point is that charge storage is not purely EDLC; it involves fast faradaic reactions that can still look quasi-rectangular in CV when kinetics are favorable and films are thin.

A common expression used for Na^+-compensated pseudocapacitance is

$$MnO_2 + Na^+ + e^- \rightleftharpoons MnOONa \quad (3)$$

and, as above, a proton-coupled representation like (2) is also used.

These "mild electrolyte" pseudocapacitive concepts (cation-assisted redox with Mn valence change) are summarized clearly in mechanistic discussions of MnO_2 capacitors [15,29]. Experimentally, MnO_2 performance in neutral sulfate electrolytes has been widely reported; for example, MnO_2 nanorods tested in $Li_2SO_4/Na_2SO_4/K_2SO_4$ show capacitive behavior strongly dependent on the identity of the electrolyte cation, consistent with a cation-involved mechanism rather than purely EDLC [31]. The absence of pseudocapacitance peaks in CV plots for Na_2SO_4 may suggest that surface adsorption may be the possible cause, which was also demonstrated earlier [29].

When $K_3[Fe(CN)_6]$ is added to Na_2SO_4, the electrolyte becomes redox-active due to the reversible ferricyanide/ferrocyanide couple:

$$\left[\mathrm{Fe}\left(\mathrm{CN}\right)_6\right]^{3-} + \mathrm{e}^- \rightleftharpoons \left[\mathrm{Fe}\left(\mathrm{CN}\right)_6\right]^{4-} \quad (4)$$

This reaction provides an additional faradaic charge-storage pathway in the electrolyte itself. In such systems, the measured charge during GCD (and sometimes CV at sufficiently slow scan rates) is no longer attributable solely to MnO_2 (or carbon) pseudocapacitance/EDLC; instead, it becomes a hybrid of electrode pseudocapacitance and electrolyte redox charge. The role of $K_3[Fe(CN)_6]$ as a redox additive that enhances apparent capacitance/energy density in aqueous supercapacitors is widely documented and reviewed [21,31,32].

In the presence of MnO_2, two coupled processes occur during charge/discharge, similar to the reactions provided in (2) and (3) above. However, an electrolyte redox mediation (ferricyanide/ferrocyanide) happens as follows:

$$\left[\mathrm{Fe}\left(\mathrm{CN}\right)_6\right]^{3-} + \mathrm{e}^- \rightleftharpoons \left[\mathrm{Fe}\left(\mathrm{CN}\right)_6\right]^{4-} \quad (5)$$

The ferri/ferrocyanide couple can act as a redox shuttle/charge buffer, enabling extra charge to be stored and released through reversible solution-phase redox. This can (a) increase apparent capacitance, (b) reduce polarization in some regimes by improving effective charge-transfer kinetics, and (c) strongly accentuate time-scale effects, which is why many systems show much larger "capacitance" in GCD than CV when redox additives are present [21,22,33]. A clear example of $K_3[Fe(CN)_6]$ boosting performance in aqueous supercapacitors is reported for symmetric devices in Na_2SO_4 with a ferricyanide additive, where the additive increases electrolyte conductivity and adds faradaic charge storage through the $Fe(CN)_6{}^{3-/4-}$ couple. Recent reviews also summarize ferricyanide as one of the most commonly used redox additives in neutral aqueous electrolytes for supercapacitors.

The specific capacitance originated from the CV plots can be calculated as

$$C = \frac{A}{2m\,k\,\Delta v} \quad (6)$$

where C = specific capacitance (F/g);

A = area of the CV plot (A.V);

m = mass of active material in the electrode (g);

k = scan rate (V/s);

Δv = potential window of voltage sweep (V).

The specific capacitance as a function of carbon percent in the composite electrodes is shown in Figure 6a–c for KOH and Na_2SO_4 and a mixture of Na_2SO_4 and $K_3[Fe(CN)_6]$ as electrolytes, respectively. In such CV-based capacitance, KOH-based electrolytes demonstrate the highest specific capacitance values, and the capacitance increases with the increase in carbon content. Such behavior suggests that carbon contributes more to the specific capacities compared to the MnO_2, and hence MnO_2 does not have an influence. However,

a different scenario is observed for the remaining two electrolytes. For all scan rates and for the two remaining electrolytes, specific capacitance is very low for pure MnO_2, increases with the increase in porous carbon content, and then decreases.

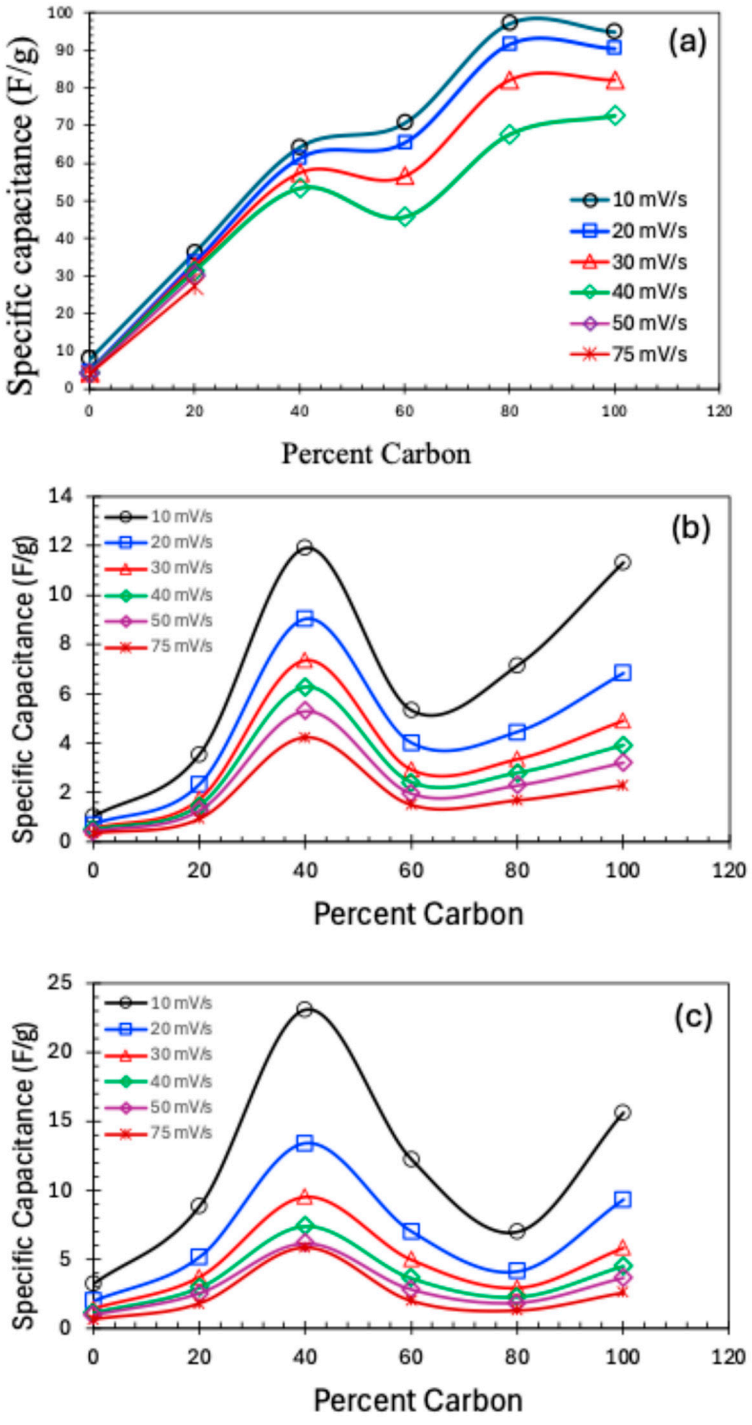

Figure 6. Specific capacitance originated from cyclic voltammetry plots in three different electrolytes: (**a**) 6 M KOH, (**b**) 1 M Na_2SO_4, (**c**) a mixture of 1 M Na_2SO_4 and 0.03 M $K_3[Fe(CN)_6]$. The specific capacitance at the larger scan rates for KOH has been removed as the CV plot was truncated owing to the limiting current of the instrument.

In contrast to MnO_2, porous carbon possesses high electronic conductivity and extensive accessible surface area, enabling rapid electron transport and efficient formation of the electric double layer. Consequently, pure porous carbon electrodes typically exhibit

higher specific capacitance than pure MnO_2, even though MnO_2 has a higher theoretical capacitance. This apparent contradiction arises because the theoretical pseudocapacitance of MnO_2 is rarely achieved in practice due to poor conductivity, slow ion diffusion, and incomplete utilization of the bulk material. When MnO_2 is introduced into a porous carbon matrix, the system becomes electronically heterogeneous. During CV measurements, which rely on rapid potential sweeps, electron transport through MnO_2 domains becomes rate-limiting. Even though the surrounding carbon network is highly conductive, electrons must still traverse MnO_2 regions to access pseudocapacitive sites. This leads to significant polarization and incomplete redox utilization of MnO_2 during CV, particularly at practical scan rates. When mixed with carbon, the conductive carbon framework acts as an efficient current collector, enabling MnO_2 particles to participate more fully in faradaic charge storage. The composite of 40% carbon/60% MnO_2 demonstrated the highest specific capacitance values. The superior electrochemical performance observed for the composite containing 40% nanoporous carbon and 60% MnO_2 might have resulted from an optimal balance between electronic conductivity, ion-transport pathways, and utilization of MnO_2 surface sites. At 40% carbon content, this conductive network becomes sufficiently interconnected to effectively "wire" the MnO_2 domains, allowing the majority of MnO_2 surface sites to participate in fast charge storage. The decrease in specific capacitance at the higher scan rates is a common observation. At higher scan rates, the applied voltage changes faster than ions can diffuse into the micro- and mesoporous networks of the carbon. As a result, charge storage becomes confined mainly to the external surface or larger pores. This limited ionic access leads to incomplete charging and a reduced current response, which in turn lowers specific capacitance and distorts the cyclic voltammetry (CV) profile.

The galvanostatic charge–discharge (GCD) profiles are shown in Figure 7a–c for KOH and Na_2SO_4 and a mixture of Na_2SO_4 and $K_3[Fe(CN)_6]$ as electrolytes, respectively. The specific capacitance from GCD plots can be calculated as

$$C = \frac{I_m \Delta t}{\Delta v} \tag{7}$$

where C = specific capacitance (F/g);

I_m = current density (current/mass of electrode material) (A/g);

Δt = discharge time (s);

Δv = potential window of charging and discharging (V).

The energy density (E_g) and power density (P_g) can be calculated using the following relations:

$$E_g = \frac{1}{2} C V^2 \tag{8}$$

where E_g = energy density (Wh/kg);

C = specific capacitance (F/g);

V = potential window of charging and discharging (V).

$$P_g = \frac{E}{\Delta t} \tag{9}$$

where P = energy density (W/kg);

Δt = time of discharge (s).

The specific capacitance derived from GCD and E_g as a function of carbon contents are shown in Figure 8a–c for KOH and Na_2SO_4 and a mixture of Na_2SO_4 and $K_3[Fe(CN)_6]$ as electrolytes, respectively.

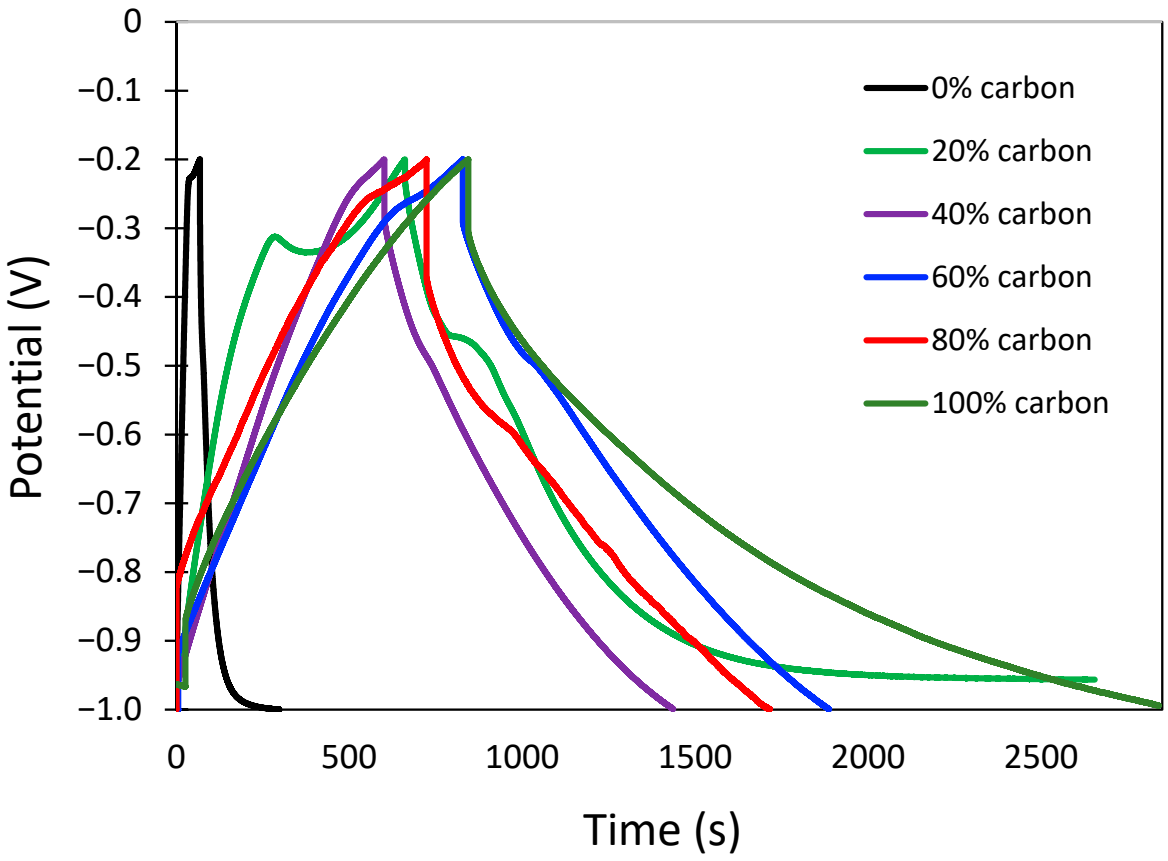

(**a**)

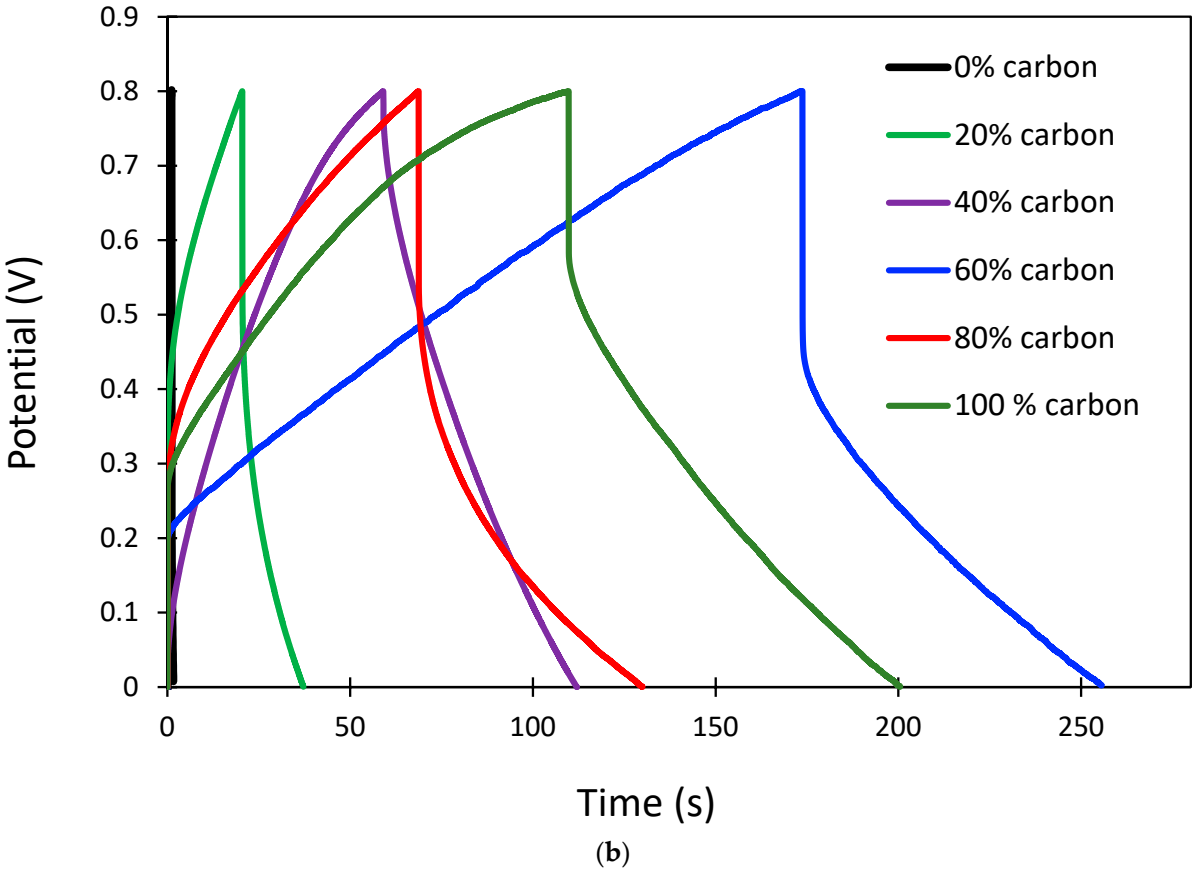

(**b**)

Figure 7. *Cont.*

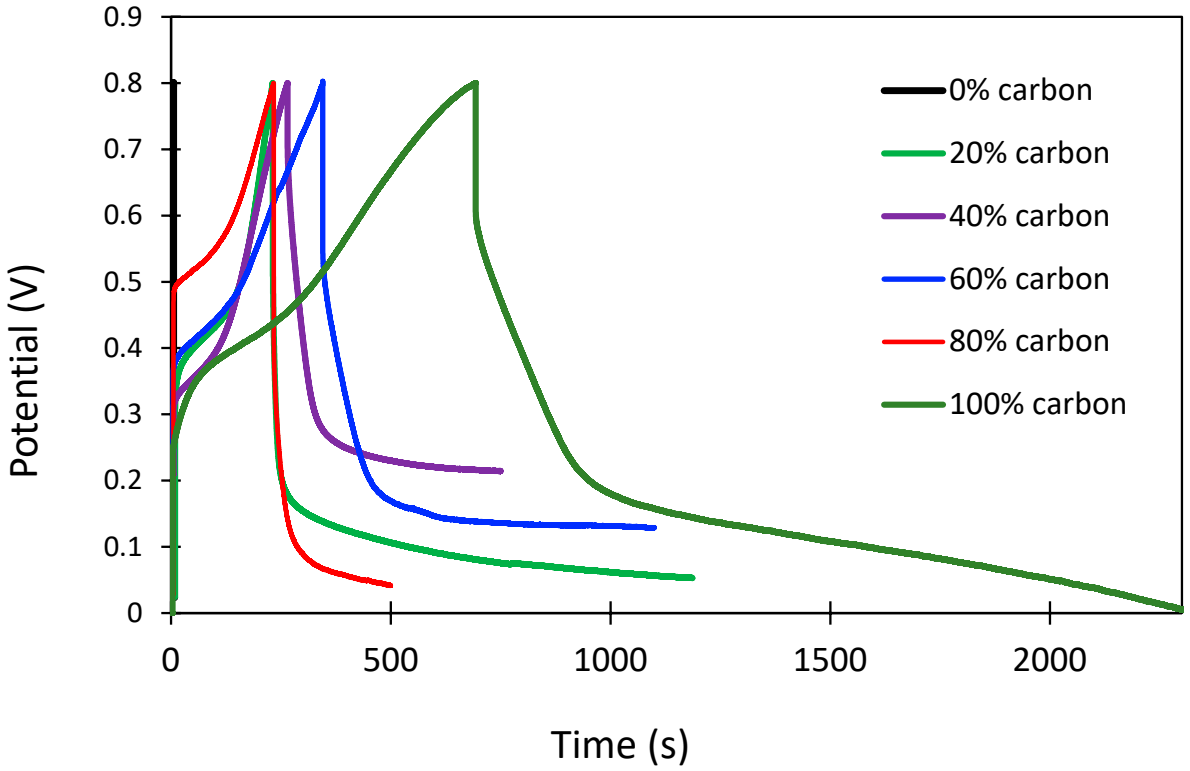

(**c**)

Figure 7. (**a**) Galvanostatic charge–discharge (GCD) plots for KOH as electrolyte. (**b**) Galvanostatic charge–discharge (GCD) plots for Na_2SO_4 as electrolyte. (**c**) Galvanostatic charge–discharge (GCD) plots for the mixture of Na_2SO_4 and $K_3[Fe(CN)_6]$ as electrolyte.

In the galvanostatic charge–discharge (GCD) measurements and for Na_2SO_4 and $Na_2SO_4/K_3[Fe(CN)_6]$, the electrode containing 40% carbon also exhibits the most ideal triangular profile characteristic of double-layer capacitance, with minimal voltage distortion and the smallest iR drop. This further confirms the formation of a highly efficient and continuous conductive network at this composition. When the carbon content is below 40%, the MnO_2-rich electrodes become electronically resistive, resulting in significant internal voltage loss at the beginning of each charge–discharge step and yielding a pronounced iR drop. The high resistive contribution also distorts the shape of the GCD curves, producing asymmetry and curvature consistent with sluggish electronic transport and kinetically limited redox reactions. Conversely, when the carbon content is too high, although electronic resistance is low, the effective amount of MnO_2 contributing to charge storage becomes diluted, leading to lower overall capacitance. The near-ideal GCD behavior at 40% carbon, therefore, reflects the optimal balance between high conductivity and sufficient MnO_2 loading, allowing charge to be stored and released uniformly across the electrode with minimal resistive losses. This observation aligns with the CV and EIS data and further demonstrates that 40% carbon/60% MnO_2 is the composition that maximizes electrochemical performance in this system.

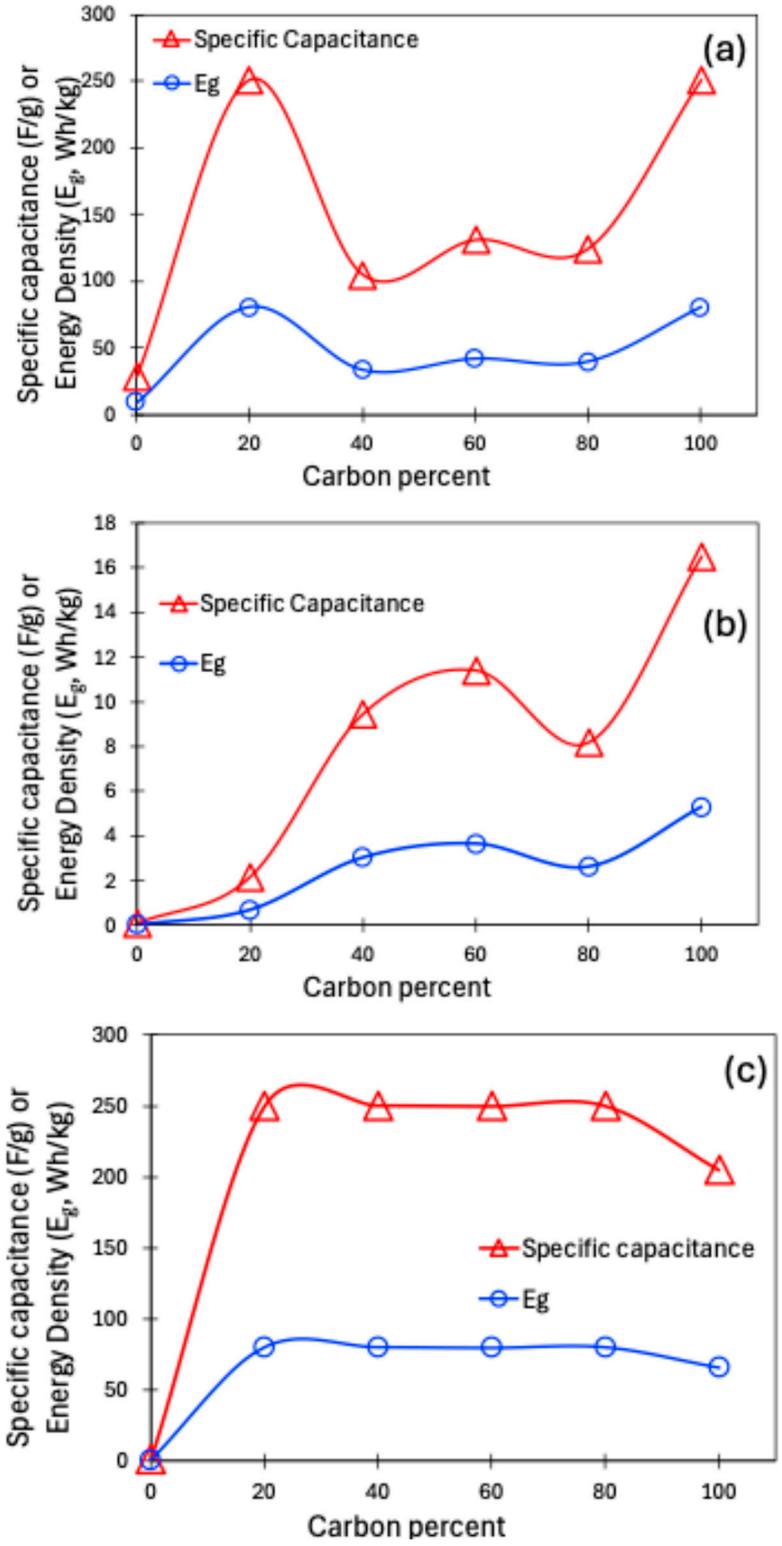

Figure 8. Specific capacitance originated from GCD and energy density (E_g) as a function of carbon content in the electrode for (**a**) KOH, (**b**) Na_2SO_4, and (**c**) mixture of Na_2SO_4 and $K_3[Fe(CN)_6]$ as electrolyte.

For the KOH-based electrolyte, the specific capacitance calculated from the GCD plot is around 250 F/g, which is a 20% carbon/80% MnO_2 composite and is similar to 100% carbon. This is significantly higher than that measured by cyclic voltammetry. The energy density (E_g) has a similar variation with a maximum value of 80 Wh/kg. For the Na_2SO_4-based electrolyte, the highest specific capacitance is around 12–15 F/g, which is

in a similar range to that obtained from CV plots. The energy density follows a similar pattern, with the values within 4–6 Wh/kg. A completely different pattern is observed for a mixture of Na_2SO_4 and $K_3[Fe(CN)_6]$ as electrolyte. A very high specific capacitance is obtained, around 240–250 F/g, within a carbon percentage of 40–80%. This value is one order of magnitude higher than that obtained from a CV plot for the same electrolyte. The energy density also follows the same trend, with values from 60 to 80 Wh/kg. Since all the GCD experiments for Na_2SO_4 and a mixture of Na_2SO_4 and $K_3[Fe(CN)_6]$ as electrolytes were performed at the same current density (0.1 A/g) and potential window (0.8 V), the power density (P_g) attained the same value of 0.04 Wh/Kg.

Cyclic voltammetry probes the electrochemical response over a relatively short time scale, particularly at moderate to high scan rates. In porous electrodes dominated by micropores, ion transport into the internal pore network becomes rate-limiting. Hydrated Na^+ ions and, more importantly, the bulky ferricyanide/ferrocyanide ions experience steric hindrance and slow diffusion within the confined pore structure. As a result, a significant fraction of the internal surface area of the porous carbon remains electrochemically inaccessible during the CV experiment. Furthermore, MnO_2 pseudocapacitive reactions are kinetically sluggish and diffusion-controlled, leading to incomplete redox participation during rapid potential sweeps. This manifests as distorted or suppressed redox features and a reduced enclosed CV area, ultimately yielding an underestimated specific capacitance.

The presence of $K_3[Fe(CN)_6]$ further complicates the CV response. Although ferricyanide is electrochemically active, its redox contribution is not fully captured in CV unless extremely low scan rates are employed. At typical scan rates, the electron transfer and mass transport of the ferricyanide/ferrocyanide couple cannot keep pace with the changing potential, resulting in partial utilization of the redox species. Consequently, CV predominantly reflects the EDLC contribution of the carbon and only a fraction of the MnO_2 pseudocapacitance and electrolyte redox charge. This explains the low apparent capacitance values obtained from CV measurements. In addition, it should also be noted that when a redox-active electrolyte such as $K_3[Fe(CN)_6]$ is introduced, an additional faradaic charge-storage pathway becomes available via the reversible $Fe(CN)_6^{3-}/Fe(CN)_6^{4-}$ redox couple. Consequently, the total stored charge is no longer solely a property of the electrode material but also includes a substantial contribution from the electrolyte itself.

In contrast, galvanostatic charge–discharge measurements are performed over significantly longer time scales and under a constant current condition. This allows sufficient time for ions to diffuse into the porous network and for faradaic reactions to proceed toward completion. During GCD, the ferricyanide/ferrocyanide redox couple acts as a charge reservoir, continuously accepting and donating electrons throughout the charge and discharge processes. This leads to prolonged discharge times and a substantial increase in the measured charge passed through the system. When the discharge time is inserted into the standard capacitance equation, the additional faradaic charge originating from electrolyte redox reactions is interpreted as an increase in capacitance. Moreover, the longer time scale of GCD allows more complete utilization of MnO_2 pseudocapacitance, including ion insertion and surface redox processes that are otherwise kinetically limited in CV. As a result, GCD measurements reflect the combined contributions of EDLC, MnO_2 pseudocapacitance, and electrolyte-mediated redox charge storage. The measured capacitance, therefore, represents an apparent or effective capacitance rather than the intrinsic capacitance of the electrode material alone. The pronounced tailing observed in the GCD curves, particularly in the $Na_2SO_4/K_3[Fe(CN)_6]$ electrolyte, arises from electrolyte-mediated faradaic redox processes in addition to capacitive charge storage. The $Fe(CN)_6^{3-}/Fe(CN)_6^{4-}$ redox couple contributes on a longer time scale than electric double-layer charging, resulting in extended discharge times and an apparent Coulombic efficiency exceeding 100%. This behavior does

not indicate enhanced energy efficiency but reflects delayed utilization of redox-active species and pseudocapacitive MnO_2 during discharge.

It is important to emphasize that CV and GCD are not equivalent techniques in systems involving redox-active electrolytes and diffusion-controlled pseudocapacitive materials. CV provides insight into kinetic limitations and accessible surface area under dynamic conditions, whereas GCD captures the maximum charge-storage capability under quasi-steady-state conditions. The large discrepancy observed in the present study indicates that the electrode–electrolyte system behaves as a hybrid or redox-mediated supercapacitor rather than a purely electrostatic capacitor. The reason for such behavior lies in the electronic conductivity mismatch, interfacial charge-transfer resistance, and utilization efficiency of the electrochemically active mass. These factors strongly influence how CV and GCD probe the electrode, particularly in composite systems where a poorly conducting pseudocapacitive phase is dispersed within a highly conductive carbon matrix.

It should be noted that the individual contributions of PET-derived carbon and MnO_2 within the composite cannot be rigorously deconvoluted, as strong synergistic interactions between the two components lead to coupled charge-storage behavior. Meaningful comparison of individual contributions is therefore limited to the respective single-component electrodes, while the composite response reflects an interdependent, electrolyte-dependent mechanism.

The electrochemical impedance spectroscopy (EIS) data are shown in Figures 9–11 for KOH and Na_2SO_4 and a mixture of Na_2SO_4 and $K_3[Fe(CN)_6]$ as electrolytes, respectively. For the Nyquist plots shown in Figures 9a, 10a and 11a and at the high-frequency region, the size of the semicircular feature reflects the electron transport involved in faradaic processes, quantified by the charge-transfer resistance (R_{ct}). This resistance is strongly influenced by the porous architecture of the carbon electrode, as it depends on both the electrolyte-accessible surface area and the intrinsic electrical conductivity of the material. For KOH and Na_2SO_4, the Nyquist plot shows the typical semicircle at high frequency and a straight line connecting at around 45° angle at low frequency, which signifies Warburg resistance and originates from the ionic diffusion within the porous electrode material. The intersection of the plot with the real axis corresponds to the equivalent series resistance (ESR), which accounts for the inherent resistance of the active carbon material, the ionic resistance of the electrolyte, and the interfacial contact resistance between the electrode and the current collector.

In the Bode plots (Figures 9b, 10b and 11b), the impedance or resistance |Z| decreases with increasing frequency; the impedance values are independent at the lower frequency and show a decreasing nature with the increase in frequency from 10 to 100 Hz. The dependence of capacitance (|C|) on frequency (Figures 9c, 10c and 11c) also exhibits two different regimes for the KOH electrolyte and mixture of Na_2SO_4 and $K_3[Fe(CN)_6]$-based electrolyte, whereas no two distinct regimes are observed for the Na_2SO_4-based electrolyte. The first zone may be attributed to the penetration of the AC signal in wider pores with the decrease in capacitance values, whereas the second zone signifies the penetration of the same signal in the narrower pores with the leveling of capacitance values [9,34]. The distributed dependence of capacitance for the Na_2SO_4-based electrolyte possibly suggests that a smaller fraction of micropores takes part in the AC response.

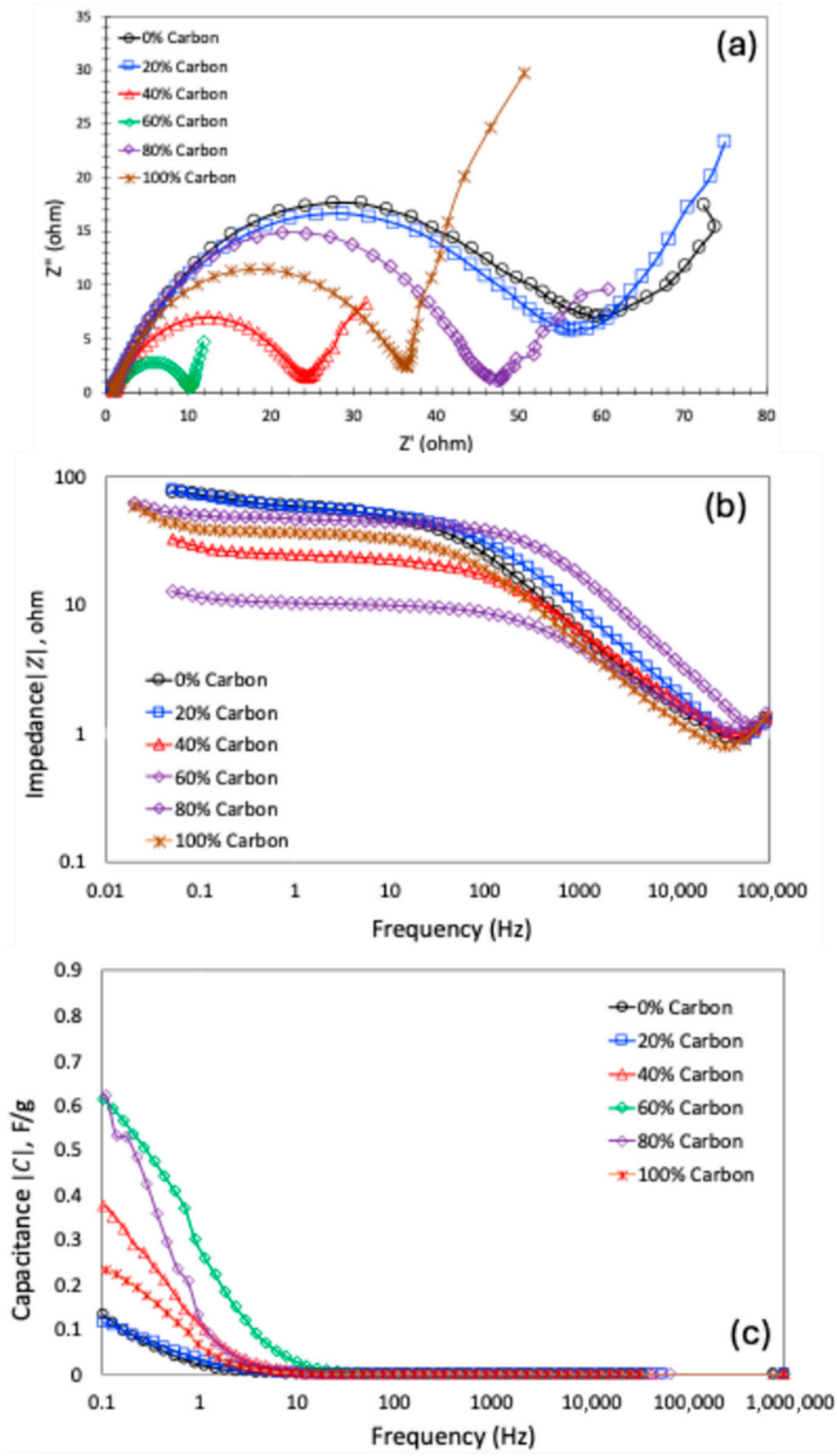

Figure 9. Electrochemical impedance spectroscopy (EIS) for KOH as electrolyte: (**a**) Nyquist plot, (**b**) Abs. impedance as a function of frequency (Bode plot), and (**c**) Abs. capacitance as a function of frequency.

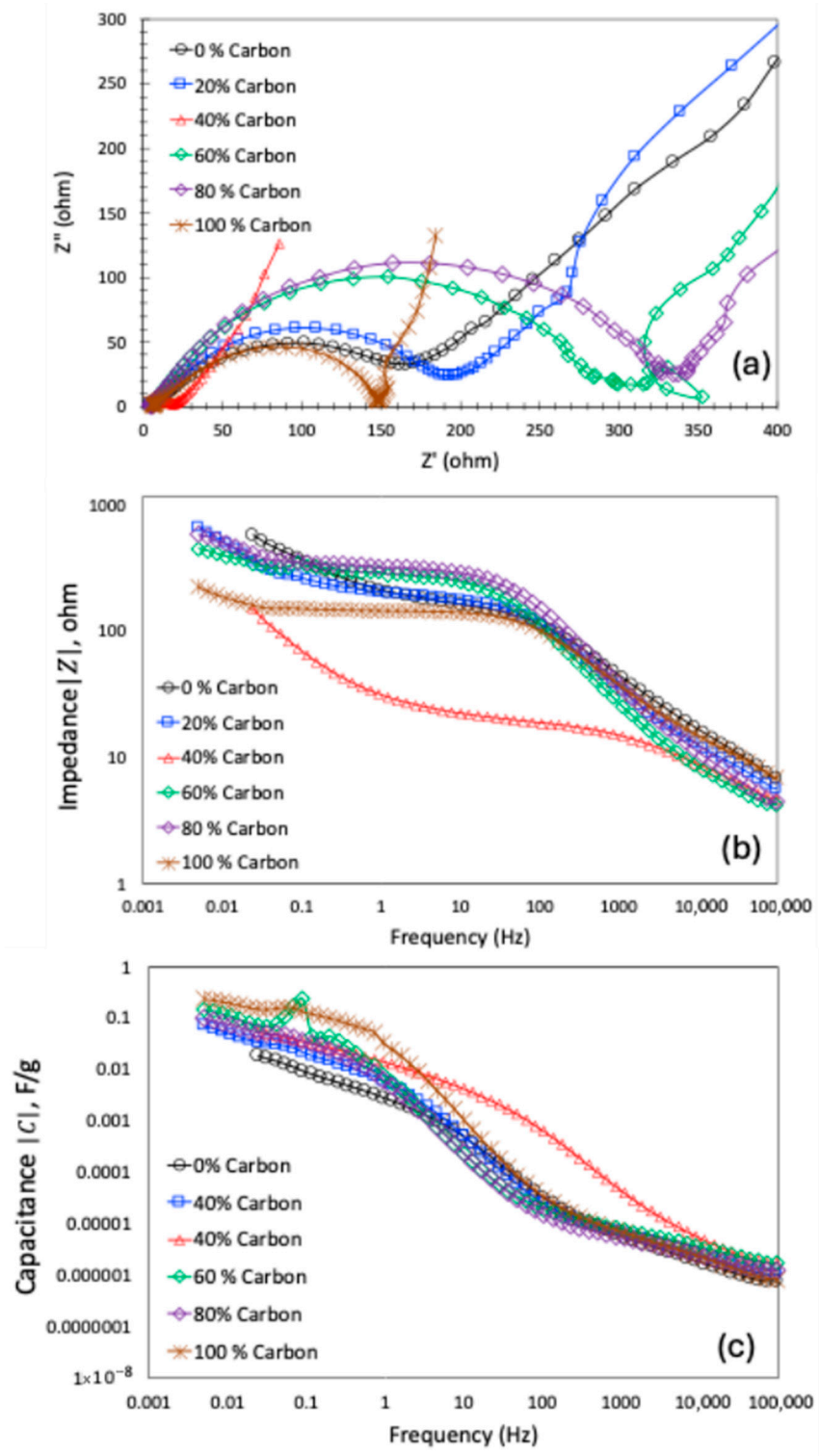

Figure 10. Electrochemical impedance spectroscopy (EIS) for Na_2SO_4 as electrolyte: (**a**) Nyquist plot, (**b**) Abs. impedance as a function of frequency (Bode plot), and (**c**) Abs. capacitance as a function of frequency.

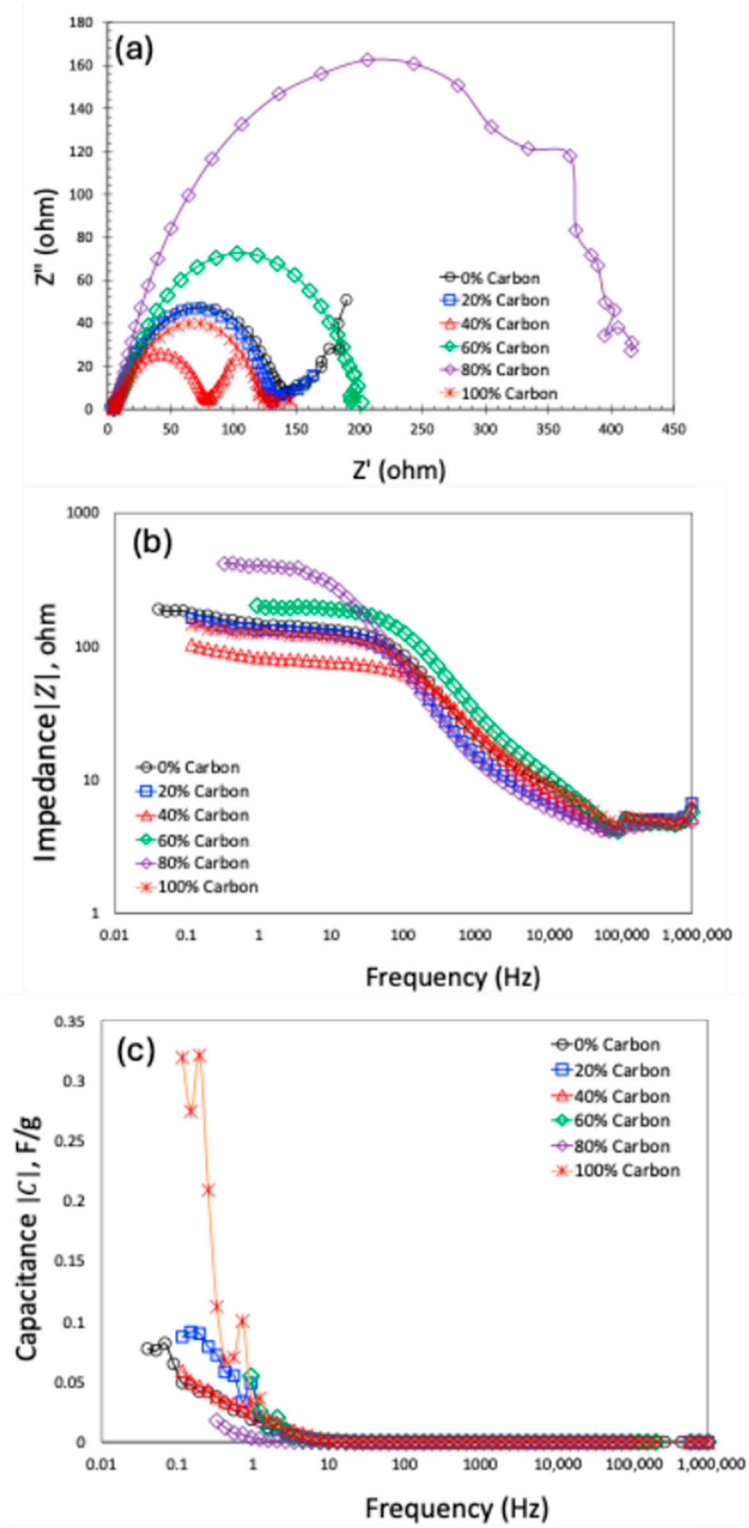

Figure 11. Electrochemical impedance spectroscopy (EIS) for a mixture of Na_2SO_4 and $K_3[Fe(CN)_6]$ as electrolyte: (**a**) Nyquist plot, (**b**) Abs. impedance as a function of frequency (Bode plot), and (**c**) Abs. capacitance as a function of frequency.

It is observed that for a mixture of Na_2SO_4 and $K_3[Fe(CN)_6]$ a electrolyte, the straight line (Warburg resistance) is very noisy or absent in the low-frequency zone; even for 60% carbon/40% MnO_2, the end of the semicircle, at the relatively lower frequency, also becomes noisy. In conventional supercapacitors using inert electrolytes, the 45° line in the Nyquist plot is associated with semi-infinite linear diffusion of ions within porous

electrodes (Warburg impedance). However, when a redox-active species such as the ferricyanide/ferrocyanide couple is present, the low-frequency impedance response no longer reflects simple ion diffusion. The reversible redox reaction (Equation (5)) introduces faradaic charge transfer and diffusion of redox species in the electrolyte, which competes with or dominates over classical ion diffusion in the electrode pores. Under these conditions, the impedance response transitions from diffusion-controlled Warburg behavior to finite-length diffusion and redox-reaction-limited behavior, which does not yield a clean 45° line [35,36]. The pronounced noise observed in the low-frequency region of the Nyquist plot is a known consequence of non-stationary electrochemical processes. Electrochemical impedance spectroscopy formally assumes that the system is linear, time-invariant, and at steady state. Redox-active electrolytes violate these assumptions because the concentration of ferricyanide and ferrocyanide near the electrode surface changes dynamically during the AC perturbation, particularly at low frequencies where the perturbation period is long. As a result, the impedance response becomes unstable and noisy due to slow diffusion of bulky $Fe(CN)_6^{3-}/^{4-}$ ions, local depletion and regeneration of redox species, and coupling between solution-phase diffusion and electrode kinetics. Such low-frequency noise in redox-mediated systems has been widely reported and is often interpreted as a signature of pseudocapacitive or battery-like behavior rather than ideal capacitive behavior [37–39]. Additionally, ferricyanide and ferrocyanide ions are large, multivalent species, and their diffusion into micropores is severely hindered. In porous carbon/MnO_2 composites, especially those with high carbon fractions and microporosity, this leads to partial pore blocking, non-uniform ion accessibility, and spatially heterogeneous impedance response. Therefore, instead of a smooth Warburg diffusion tail, the impedance spectrum exhibits scattered points and noise, reflecting stochastic access of redox species to electrochemically active sites. Similar deviations from ideal Warburg behavior in porous carbons with redox electrolytes have been discussed in the context of pore-size/ion-size mismatch [40,41]. Therefore, taken together, the absence of a clear 45° Warburg line, the emergence of low-frequency noise, and the instability at the end of the semicircle in Na_2SO_4 + $K_3[Fe(CN)_6]$ electrolyte are hallmarks of a redox-mediated hybrid charge-storage mechanism. The system no longer behaves as an ideal supercapacitor governed by ion diffusion alone; instead, it exhibits characteristics of a mixed capacitive–faradaic system, where electrolyte redox reactions, finite-length diffusion, and interfacial instabilities dominate the low-frequency impedance response.

The Nyquist plot is fitted into a simple Randles circuit (Figure S1) using the built-in software of the instrument, and the resultant fitting parameters are shown in Figure S2 of the Supplementary Information.

4. Conclusions

PET-derived porous carbons were synthesized with a highly microporous structure and characterized by porosity, X-ray diffraction and SEM-EDX. The carbon was successfully utilized as a conductive scaffold for MnO_2 to fabricate hybrid supercapacitor electrodes, providing a sustainable pathway for converting plastic waste into functional energy-storage materials. The electrochemical performance of the composites was strongly dependent on both electrode composition and electrolyte chemistry. An optimal balance between electronic conductivity and MnO_2 loading was achieved at approximately 40% carbon content, resulting in superior capacitive behavior and minimal internal resistance. In KOH electrolyte, MnO_2 exhibited clear pseudocapacitive characteristics associated with fast surface redox reactions, whereas in Na_2SO_4, the charge storage was primarily governed by electric double-layer capacitance with relatively low specific capacitance. The incorporation of $K_3[Fe(CN)_6]$ into Na_2SO_4 fundamentally altered the charge-storage mechanism,

leading to redox-mediated behavior characterized by high apparent capacitance and energy density in galvanostatic measurements but pronounced discrepancies with cyclic voltammetry results. Electrochemical impedance spectroscopy revealed that redox-active electrolytes disrupt classical diffusion-controlled impedance responses, producing noisy low-frequency behavior and ill-defined Warburg regions. These findings demonstrate that CV, GCD, and EIS probe different aspects of hybrid electrode–electrolyte systems and must be interpreted carefully, particularly in the presence of redox additives. Overall, this work provides mechanistic insight into PET-derived carbon/MnO_2 hybrid electrodes and establishes electrolyte-dependent design and interpretation guidelines for developing high-performance, sustainable supercapacitors.

Supplementary Materials: The following supporting information can be downloaded at https://www.mdpi.com/article/10.3390/surfaces9020041/s1, Figure S1: Randles Circuit; Figure S2: Dependance of R1 (a), R2 (b), W(c) and C (d) on the carbon percentage of the active materials of the electrode; Figure S3: Galvanostatic Charge-Discharge (GCD) plots for KOH as electrolyte for different carbon percent; Figure S4: Galvanostatic Charge-Discharge (GCD) plots for Na_2SO_4 as electrolyte for different carbon percent; Figure S5: Galvanostatic Charge-Discharge (GCD) plots for the mixture of Na_2SO_4 and $K_3[Fe(CN)_6]$ as electrolyte for different carbon percent.

Author Contributions: Conceptualization, D.S.; Methodology, D.S., L.L., K.W.K. and C.M.B.; Software, D.S., L.L. and C.M.B.; Validation, D.S. and L.L.; Formal analysis, L.L.; Investigation, D.S., L.L., K.W.K. and C.M.B.; Resources, D.S.; Data curation, D.S.; Writing—original draft, D.S.; Writing—review & editing, D.S.; Visualization, K.W.K.; Supervision, D.S.; Project administration, D.S.; Funding acquisition, D.S. All authors have read and agreed to the published version of the manuscript.

Funding: This research received no external funding.

Data Availability Statement: No additional data is available beyond Supplemental Information.

Acknowledgments: L.L. acknowledges the support from the School of Engineering of Widener University. D.S. acknowledges the Fred A. Akl Endowed Engineering Professorship from Widener University. K.W.K. acknowledges support from the US National Science Foundation (NSF) Major Research Instrumentation (MRI) program under award number 2216272.

Conflicts of Interest: The authors declare no conflict of interest.

References

1. Bassi, S.A.; Tonini, D.; Saveyn, H.; Astrup, T.F. Environmental and Socioeconomic Impacts of Poly(ethylene terephthalate) (PET) Packaging Management Strategies in the EU. *Environ. Sci. Technol.* **2022**, *56*, 501–511.
2. Joseph, T.M.; Azat, S.; Ahmadi, Z.; Jazani, O.M.; Esmaeili, A.; Kianfar, E.; Haponiuk, J.; Thomas, S. Polyethylene terephthalate (PET) recycling: A review. *Case Stud. Chem. Environ. Eng.* **2024**, *9*, 100673.
3. Bhanderi, K.K.; Joshi, J.R.; Patel, J.V. Recycling of polyethylene terephthalate (PET or PETE) plastics—An alternative to obtain value added products: A review. *J. Indian Chem. Soc.* **2023**, *100*, 100843. [CrossRef]
4. Guo, Z.; Wu, J.; Wang, J. Chemical degradation and recycling of polyethylene terephthalate (PET): A review. *RSC Sustain.* **2025**, *3*, 2111. [CrossRef]
5. Wang, S.; Dou, J.; Holze, R.; Zhang, T.; Ye, L.; Duan, L.; Xue, J.; Li, S.; Chen, X. Recent Progress in Polymer Waste-Derived Porous Carbon for Supercapacitors. *ChemElectroChem* **2023**, *10*, e202300223.
6. Zhai, Z.; Zhang, L.; Du, T.; Ren, B.; Xu, Y.; Wang, S.; Mia, J.; Liu, Z. A review of carbon materials for supercapacitors. *Mater. Des.* **2022**, *221*, 111017. [CrossRef]
7. Patial, S.K.; Shavita; Singh, S. Waste PET bottles derived carbon black as electrode material for supercapacitor application. *Mater. Lett.* **2024**, *371*, 136976. [CrossRef]
8. Choi, J.; Jung, W.; Jung, J.C. Efficient production of activated carbons from PET for organic supercapacitor applications: A single-step approach. *Mater. Res. Bull.* **2025**, *182*, 113166. [CrossRef]

9. Saha, D.; Li, Y.; Bi, Z.; Chen, J.; Keum, J.K.; Hensley, D.K.; Grappe, H.A.; Meyer, H., III; Dai, S.; Paranthaman, M.P.; et al. Studies on supercapacitor electrode material from activated lignin derived mesoporous carbon material. *Langmuir* **2014**, *30*, 900–910. [CrossRef] [PubMed]
10. Saha, D.; Ruggiero, A.; Gittinger, S.; Mallouhi, F.; Gross, M. Thermo-chemical conversion of PET-based plastic wastes to activated carbons: Role in supercapacitors in aqueous and organic electrolytes. *Waste Manag.* **2026**, *210*, 115255. [CrossRef]
11. Mu, X.; Li, Y.; Liu, X.; Ma, C.; Jiang, H.; Zhu, J.; Chen, X.; Tang, T.; Mijowska, E. Controllable Carbonization of Plastic Waste into Three-Dimensional Porous Carbon Nanosheets by Combined Catalyst for High Performance Capacitor. *Nanomaterials* **2020**, *10*, 1097. [CrossRef]
12. Liu, J.; Bao, J.; Zhang, X.; Gao, Y.; Zhang, Y.; Liu, L.; Cao, Z. MnO_2-based materials for supercapacitor electrodes: Challenges, strategies and prospects. *RSC Adv.* **2022**, *12*, 35556. [CrossRef]
13. Devi, R.; Kumar, V.; Kumar, S.; Bulla, M.; Sharma, S.; Sharma, A. Electrochemical Analysis of MnO_2 (α, β, and γ)-Based Electrode for High-Performance Supercapacitor Application. *Appl. Sci.* **2023**, *13*, 7907. [CrossRef]
14. Toupin, M.; Brousse, T.; Bélanger, D. Charge Storage Mechanism of MnO_2 Electrode Used in Aqueous Electrochemical Capacitor. *Chem. Mater.* **2004**, *16*, 3184–3190. [CrossRef]
15. Hung, S.-C.; Chou, Y.-R.; Dong, C.-D.; Tsai, K.-C.; Yang, W.-D. Enhanced Activity of Hierarchical Nanostructural Birnessite-MnO_2-Based Materials Deposited onto Nickel Foam for Efficient Supercapacitor Electrodes. *Nanomaterials* **2020**, *10*, 1933. [CrossRef]
16. Sangeetha, D.; Santosh, M.; Selvakumar, M. Flower-like carbon doped MoS_2/Activated carbon composite electrode for superior performance of supercapacitors and hydrogen evolution reactions. *J. Alloys Compd.* **2020**, *831*, 154745. [CrossRef]
17. Sakib, M.N.; Ahmed, S.; Rahat, S.M.S.M.; Shuchi, S.B. A review of recent advances in manganese-based supercapacitors. *Energy Storage* **2021**, *44*, 103322. [CrossRef]
18. Wu, D.; Xie, X.; Zhang, Y.; Zhang, D.; Du, W.; Zhang, X.; Wang, B. MnO_2/Carbon Composites for Supercapacitor: Synthesis and Electrochemical Performance. *Front. Mater.* **2020**, *7*, 2. [CrossRef]
19. Diantoro, M.; Istiqomah, I.; Al Fath, Y.; Nasikhudin, N.; Alias, Y.; Meevasana, W. Potential of MnO_2-based composite and numerous morphological for enhancing supercapacitors performance. *Int. J. Appl. Ceram. Technol.* **2023**, *20*, 2077–2098. [CrossRef]
20. Lee, J.; Choudhury, S.; Weingarth, D.; Kim, D.; Presser, V. High Performance Hybrid Energy Storage with Potassium Ferricyanide Redox Electrolyte. *ACS Appl. Mater. Interfaces* **2016**, *8*, 23676–23687. [CrossRef]
21. Guan, L.; Guo, L.; Yao, H.; Cai, J.; Dong, X.; Wang, R.; Zhai, Z.; Chen, X.; Wei, X.; Li, D.; et al. Redox Additive Electrolytes for Supercapacitors: A Mini-Review on Recent Developments and Future Directions. *Molecules* **2025**, *30*, 1764. [CrossRef]
22. Shrivastav, V.; Dubey, P.; Bakandritsos, A.; Sundriyal, S.; Tiwari, U.; Deep, A. High performance supercapacitors driven by the synergy of a redox-active electrolyte and core–nanoshell zeolitic imidazolate frameworks. *Nanoscale Adv.* **2025**, *7*, 2105.
23. Chen, K.; Song, S.; Xue, D. An ionic aqueous pseudocapacitor system: Electroactive ions in both a salt electrode and redox electrolyte. *RSC Adv.* **2014**, *4*, 23338. [CrossRef]
24. Arkhipova, E.A.; Ivanov, A.S.; Maslakov, K.I.; Novotortsev, R.Y.; Savilov, S.V.; Xia, H.; Aldoshin, S.M. Boosting MnO_2-specific capacitance via surfactant-assisted synthesis and employing redox-active electrolyte. *Ionics* **2024**, *30*, 1125–1136. [CrossRef]
25. Saha, D.; Schlosser, R.; Lapointe, L.; Comroe, M.L.; Samohod, J.; Whiting, E.; Young, D.S. Nanoporous Carbons from Hydrothermally Treated Alga: Role in Batch and Continuous Capacitive Deionization (CDI). *Molecules* **2025**, *30*, 2848. [CrossRef]
26. Saha, D.; Comroe, M.; Krishna, R.; Rascavage, M.; Larwa, J.; You, V.; Standhart, G.; Bingnear, B. Separation of propylene from propane and nitrogen by Ag(I)-doped nanoporous carbons obtained from hydrothermally treated lignin. *Diam. Relat. Mater.* **2022**, *121*, 108750. [CrossRef]
27. Saha, D.; Comroe, M.; Krishna, R. Synthesis of Cu(I) doped mesoporous carbon for selective capture of ethylene from reaction products of oxidative coupling of methane (OCM). *Microporous Mesoporous Mater.* **2021**, *328*, 111488. [CrossRef]
28. Chen, W.M.; Qie, L.; Shao, Q.G.; Yuan, L.X.; Zhang, W.X.; Huang, Y.H. Controllable synthesis of hollow bipyramid β-MnO_2 and its high electrochemical performance for lithium storage. *ACS Appl. Mater. Interfaces* **2012**, *4*, 3047–3053. [CrossRef] [PubMed]
29. Bélanger, D.; Brousse, T.; Long, J. Manganese Oxides: Battery Materials Make the Leap to Electrochemical Capacitors. *Electrochem. Soc. Interface* **2008**, *17*, 49. [CrossRef]
30. Shin, J.; Seo, J.K.; Yaylian, R.; Huang, A.; Meng, Y.S. A review on mechanistic understanding of MnO_2 in aqueous electrolyte for electrical energy storage systems. *Int. Mater. Rev.* **2020**, *65*, 356–387. [CrossRef]
31. Qu, Q.; Zhang, P.; Wang, B.; Chen, Y.; Tian, S.; Wu, Y.; Holze, R. Electrochemical Performance of MnO_2 Nanorods in Neutral Aqueous Electrolytes as a Cathode for Asymmetric Supercapacitors. *J. Phys. Chem. C* **2009**, *113*, 14020–14027. [CrossRef]
32. Sundriyal, S.; Shrivastav, V.; Kaur, H.; Mishra, S.; Deep, A. High-Performance Symmetrical Supercapacitor with a Combination of a ZIF-67/rGO Composite Electrode and a Redox Additive Electrolyte. *ACS Omega* **2018**, *3*, 17348−17358. [CrossRef] [PubMed]
33. Shi, J.; Tian, X.; Song, Y.; Yang, T.; Hu, S.; Liu, Z. Redox electrolyte-enhanced carbon-based supercapacitors: Recent advances and future perspectives. *Energy Mater. Devices* **2023**, *1*, 9370009. [CrossRef]
34. Prabaharan, S.R.S.; Vimala, R.; Zainal, Z. Nanostructured Mesoporous Carbon as Electrodes for Supercapacitors. *J. Power Sources* **2006**, *161*, 730−736. [CrossRef]

35. Conway, B.E. *Electrochemical Supercapacitors*; Kluwer/Plenum: New York, NY, USA, 1999.
36. Kötz, R.; Carlen, M. Principles and applications of electrochemical capacitors. *Electrochim. Acta* **2000**, *45*, 2483–2498. [CrossRef]
37. Lasia, A. *Electrochemical Impedance Spectroscopy and Its Applications*; Springer: Berlin/Heidelberg, Germany, 2014.
38. Macdonald, J.R.; Barsoukov, E. *Impedance Spectroscopy*; Wiley: Hoboken, NJ, USA, 2005.
39. Pech, D.; Brunet, M.; Durou, H.; Huang, P.-L.; Mochalin, V.; Gogotsi, Y.; Taberna, P.-L.; Simon, P. Ultrahigh-power micrometre-sized supercapacitors based on onion-like carbon. *J. Power Sources* **2010**, *195*, 1266–1271. [CrossRef]
40. Simon, P.; Gogotsi, Y. Capacitive energy storage in nanostructured carbon–electrolyte systems. *Acc. Chem. Res.* **2013**, *46*, 1094–1103. [CrossRef] [PubMed]
41. Chmiola, J.; Yushin, G.; Gogotsi, Y.; Portet, C.; Simon, P.; Taberna, P.L. Anomalous Increase in Carbon Capacitance at Pore Sizes Less Than 1 Nanometer. *Science* **2006**, *313*, 1760–1763. [CrossRef]

Disclaimer/Publisher's Note: The statements, opinions and data contained in all publications are solely those of the individual author(s) and contributor(s) and not of MDPI and/or the editor(s). MDPI and/or the editor(s) disclaim responsibility for any injury to people or property resulting from any ideas, methods, instructions or products referred to in the content.